Chapter 5 The High Altitude Tropical Dust Maximum

5.1 Introduction

Because it is strongly radiatively active and highly temporally and spatially variable in its abundance, suspended dust is the martian atmosphere's most meteorologically important component. Indeed, the role of dust in Mars's surface/atmosphere system is analogous to the role of water in Earth's surface/atmosphere system.

First, the more dynamic weather systems of Mars are chiefly associated with dust clouds: dust devils [*Thomas and Gierasch*, 1985; *Balme and Greeley*, 2006; *Cantor et al.*, 2006], dust "cells" [*Cantor et al.*, 2002], and dust storms at various scales [*Kahn et al.*, 1992]. Mars has carbon dioxide and water ice clouds (and the Earth has dust storms). But these types of martian clouds generally are not associated with turbulent weather at the surface, with the possible exception of carbon dioxide snow squall activity in polar night [*Colaprete et al.*, 2008].

Second, meteorological systems re-circulate dust on seasonal timescales, lifting dust from some surfaces, precipitating them upon others, and usually re-charging the original sources from the sinks [*Szwast et al.*, 2006], producing a true "dust cycle." Surface dust is both more reflective and more swiftly heated and cooled than the dark basaltic rock that makes up much of the planet's surface, providing thermal contrast between dusty "continents" and basaltic "seas" [*Zurek et al.*, 1992].

Third, the presence of a small background dust concentration in the atmosphere, which is heated strongly during the day in the visible and weakly cools in the infrared at night, enhances the static stability of the atmosphere in ways not dissimilar to water vapor in Earth's denser and more humid atmosphere [*Haberle et al.*, 1982; *Schneider*, 1983]. Mars even may have a form of dust related convection analogous to moist convection due to water on the Earth. *Fuerstenau* [2006] proposed that dust devil plumes (and potentially larger dust structures) might be so strongly heated by the sun during the day that parcels within them might be strongly positively buoyant. Such parcels might have vertical velocities of 10 ms^{-1} and reach heights of 8 km or more. This mechanism might explain the great heights reached by larger martian dust devils compared to their terrestrial analogs [*Fisher et al.*, 2005]. The production of positive buoyancy by the solar heating of dust also could explain the "puffy" dust clouds observed in intense dust storm activity that have been compared to deep moist convective "hot towers" on the Earth [*Strausberg et al.*, 2005]. Note that this effect is distinct from the positive feedback effect on winds within lower aspect ratio circulations due to dust heating [*Haberle et al.*, 1993], which does not require positive buoyancy or result in large vertical velocities.

Fourth, the contribution of dust to the lower atmospheric heat budget also has a water-related terrestrial analog. In Chapter 4, I calculated that the tropical zonal average atmospheric mass heating rates on Mars due to dust under relatively clear conditions are similar to or greater than tropical mass heating rates due to moist convective latent heat release on the Earth. Thus, if Earth is a planet defined by its hydrometeorology ("water weather"), Mars is defined by its coniometeorology ("dust weather"), the latter word being derived from the Greek word for dust, *konios*.

Accurate simulation of Mars's modern circulation, past climate, and future weather therefore is dependent on understanding the connection between the synoptic and mesoscale systems that lift and transport dust and the resulting distributions of airborne and surface dust. Modelers of the martian atmosphere have explored this connection in considerable detail, simulating dust lifting and transport with more or less parameterized routines in planetary and mesoscale models [e.g., *Murphy et al.*, 1990; *Newman et al.*, 2002a, 2002b; *Richardson and Wilson*, 2002; *Rafkin et al.*, 2002; *Basu et al.*, 2004, 2006; *Kahre et al.*, 2005, 2006, 2008].

Several datasets have been used to tune or verify these simulations. These datasets fall into two broad types: (1) nadir column opacity measurements from the surface or orbiters and (2) temperature measurements from orbit, particularly the brightness temperature near the center of the 15 micron CO_2 band, T_{15} [e.g., *Newman et al.*, 2002a; *Basu et al.*, 2004]. The first type of measurement is more sensitive to dust near the surface than dust high in the atmosphere, even though the dust high in the atmosphere still can produce significant radiative heating and cooling. The second type of measurement is more sensitive to finer aspects of the vertical structure of the dust distribution but also can be influenced by dynamical processes indirectly driven by or independent of dust heating phenomena such as water ice clouds, especially if atmospheric dust concentrations are relatively low. The logical alternative to these verification measurements is more direct observation of the vertical dust distribution through infrared or visible limb sounding.

Vertical profiles of temperature, pressure, dust, and other aerosol retrieved from observations by the Mars Climate Sounder (MCS) on Mars Reconaissance Orbiter (MRO) now provide an expansive dataset [*McCleese et al.*, 2007, 2008; *Kleinböhl et al.*, 2009] for observing the vertical structure of Mars's coniometeorological systems, evaluating present simulations of dust lifting and transport, and indicating avenues for improvement of the parameterizations used to drive these simulations.

This study is very much a first step in using the abundance of retrieved vertical profiles of dust from MCS observations to improve understanding of Mars's coniometeorology. Chapter 4 showed that the vertical and latitudinal dust distribution of Mars in northern spring and summer was very different from that generally assumed, especially by general circulation models forced by prescribed dust concentrations. The most discrepant feature is an apparent maximum in dust mass mixing ratio over the tropics during most of northern spring and summer, "the high altitude tropical dust maximum" (HATDM).

In this study, the HATDM is investigated in greater detail than Chapter 4 in order to determine its cause. In Chapter 5.2, the observed MCS dust distributions at northern summer and southern summer solstices are compared with planetary-scale simulations of active lifting and transport. In Chapter 5.3, the longitudinal structure of the HATDM and its temporal variability is investigated. In Chapter 5.4, the potential roles of dust storm activity, orographic dust lifting, pseudo-moist dust convection, and the scavenging of dust particles by water ice clouds in producing the HATDM are evaluated, and I outline what further observations and modeling work are necessary to constrain the contributions of these processes. In Chapter 5.5, I summarize the results of the study.

5.2 Comparison of MCS Vertical Dust Profiles with Simulations of Active Lifting and Transport

A number of Mars GCMs now have the capability to simulate the lifting, sedimentation, and horizontal transport of dust in Mars's atmosphere. Most modeling studies, however, have focused on the simulation of global dust storms and therefore do not describe the simulated latitudinal and vertical distribution of dust during the clear season. Two exceptions are *Richardson and Wilson* [2002], which uses the Mars GFDL model, and *Kahre et al.* [2006], which uses the Ames Mars GCM.

Figures 5.1a and 5.1b plot the nightside zonal average density-scaled opacity from nightside MCS retrievals for L_s=87.5°—92.5° and 267.5º—272.5º (hereafter L_s=90º and 270º) of MY 29 on a linear scale (cf. *Richardson and Wilson* [2002], Figures 1c-d). (See Chapter 4 for description of the retrievals, zonal averaging, and the significance of density scaled opacity.) The dust distribution observed by MCS is broadly similar to that simulated by *Richardson and Wilson* [2002] at the solstices; high concentrations of dust penetrate deeply (more deeply at southern summer solstice) into the atmosphere in the tropics and the summer hemisphere while the winter extratropics remain fairly clear. The observations at both solstices and the model simulation show regions of lower, less deeply penetrating dust in the summer mid-latitudes or near the pole, which may be attributable (in these particular simulations) to enhancement of the sedimentation of dust in the downwelling of a secondary principal meridional overturning circulation (PMOC) restricted to the summer hemisphere. The latitudes at which these features are located, however, differ between the observations and the simulation.

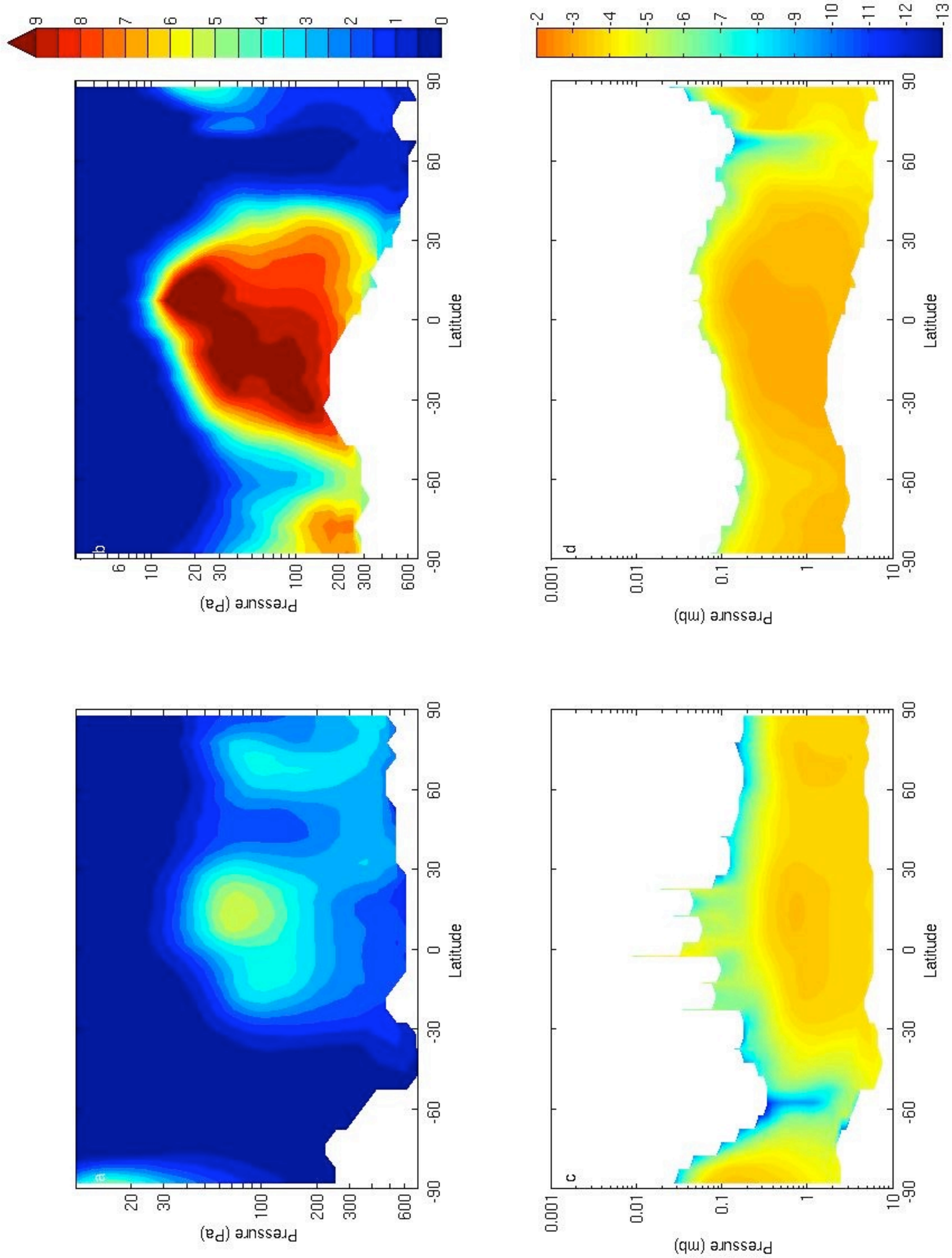

Figure 5.1. (a) Zonal average nightside dust density scaled opacity at L_s=90°, MY 29 ×10^4 m^2 kg^{-1}; (b) Zonal average nightside dust density scaled opacity at L_s=270°, MY 29 ×10^4 m^2 kg^{-1}; (c) $\log_{10}$ of zonal average nightside dust density scaled opacity at L_s=90°, MY 29 (m^2 kg^{-1}); (d) $\log_{10}$ of zonal average nightside dust density scaled opacity at L_s=270°, MY 29 (m^2 kg^{-1}).

At northern summer solstice, the observations and the GFDL model simulation disagree about the vertical dust distribution in the tropics. The simulation predicts that dust is roughly uniformly mixed to 80 Pa (perhaps at higher mass mixing ratios in the northern tropics than the southern tropics) and mass mixing ratio decays at lower pressures. MCS retrievals show that the northern and southern tropics are roughly uniformly dusty at ~300 Pa, but there is a maximum in dust mass mixing ratio at ~60 Pa over the tropics that is a little dustier in the northern than the southern tropics. This maximum is enriched by a factor of two to four over zonal average dust density scaled opacity at ~300 Pa. In other words, the model does not simulate the HATDM in the observations.

At southern summer solstice, dust density scaled opacity peaks at ~80 Pa over the equator. This maximum is broader and less enriched relative to ~300 Pa than at northern summer solstice. More poleward (between 40° S and 35° N), this maximum occurs at higher pressure levels. As at northern summer solstice (see Chapter 4), the maximum in dust density scaled opacity at the equator is vertically resolved.

Figures 5.1c-d shows the same data plotted in Figures 5.1a-b on a logarithmic scale and different pressure axes (cf. *Kahre et al.* [2006], Figures 4b and 4d). Even accounting for the broad logarithmic scale, the latitudinal-vertical structure of dust in the simulation of *Kahre et al.* [2006] differs somewhat from the simulation of *Richardson and Wilson* [2002]. But the simulation of *Kahre et al.* [2006] clearly differs from the MCS retrievals as well. *Kahre et al.* [2006] does not simulate a HATDM at northern summer solstice and appears to underestimate the clearing in the winter extratropics. Mixing ratios of ~0.1 ppm poleward of 50° S at 100 Pa are predicted by *Kahre et al.*

[2006]. However, this mass mixing ratio would correspond to a density scaled opacity of ~10^{-5} m^2 kg^{-1} (see Chapter 4 for discussion of the conversion method), which is at least an order of magnitude above what is observed in the MCS retrievals. Admittedly, the MCS retrievals have limited sensitivity at very low values of dust, but this sensitivity is on the order of 10^{-6} to 10^{-5} km^{-1}. At 100 Pa, this sensitivity corresponds to density scaled opacities on the order of 10^{-7} to 10^{-6} m^2 kg^{-1}.

In the dust distribution simulated by *Kahre et al.* [2006] at southern summer solstice, dust is uniformly mixed to 10 Pa at ~45° S and there is more dust at higher altitudes than nearer the surface over the tropics. This distribution resembles Figure 5.1b (the logarithmic scale of Figure 5.1d is insufficient to resolve it). This dust distribution may be due to cross-equatorial transport of dust from dust storm activity in the southern mid-latitudes by the PMOC, but *Kahre et al.* [2006] does not discuss this point explicitly.

In summary, the latitudinal distributions of dust simulated by *Wilson and Richardson* [2002] and *Kahre et al.* [2006] are in broad agreement with MCS observations; the tropics and the summer mid-latitudes are dustier than elsewhere on the planet. At northern summer solstice, however, both simulations fail to reproduce the zonal average vertical structure of dust in the tropics. Yet at southern summer solstice, *Kahre et al.* [2006] does simulate a vertical dust distribution fairly consistent with observations. Therefore, these two simulations incorrectly model the processes that control vertical transport of dust in the atmosphere globally in late northern spring and early northern summer but not necessarily at other seasons. The remainder of this Chapter will focus on identifying what processes may be incorrectly modeled.

5.3 The Longitudinal Structure of the HATDM

5.3.1 Approach

The catalog of processes that are capable of producing the HATDM outlined in Chapter 5.4 may not be exhaustive. Therefore, in Chapter 5.3, I will describe the longitudinal structure of the HATDM before, during, and after northern summer solstice and consider its significance with respect to simple models of sedimentation, advection, and vertical eddy diffusion. This more objective analysis will provide general observational information to evaluate explanations for the HATDM.

5.3.2 Spatial Distribution of Dust around Northern Summer Solstice

Figures 5.2a-f show nightside dust density scaled opacity around northern summer solstice of MY 29 averaged over 30º of L_s on six different σ levels, which correspond to 1, 1.5, 2, 2.5, 3, and 3.5 "scale heights" above the surface. Nearest the surface (Figure 5.2a), the northern mid-latitudes are generally less dusty than the region near the pole. In the tropics, there is some longitudinal variability in dust density scaled opacity, which resembles the thermal inertia pattern [*Putzig et al.*, 2005], though the correspondence is not exact. Note the low dust density scaled opacity over Amazonis Planitia (0°—30° N, 180°—135° W) and western Arabia Terra (0°—30° N, 0°—45° E). At this σ level (and all other levels), the region south of 30° S is generally clear of dust. The exceptions are

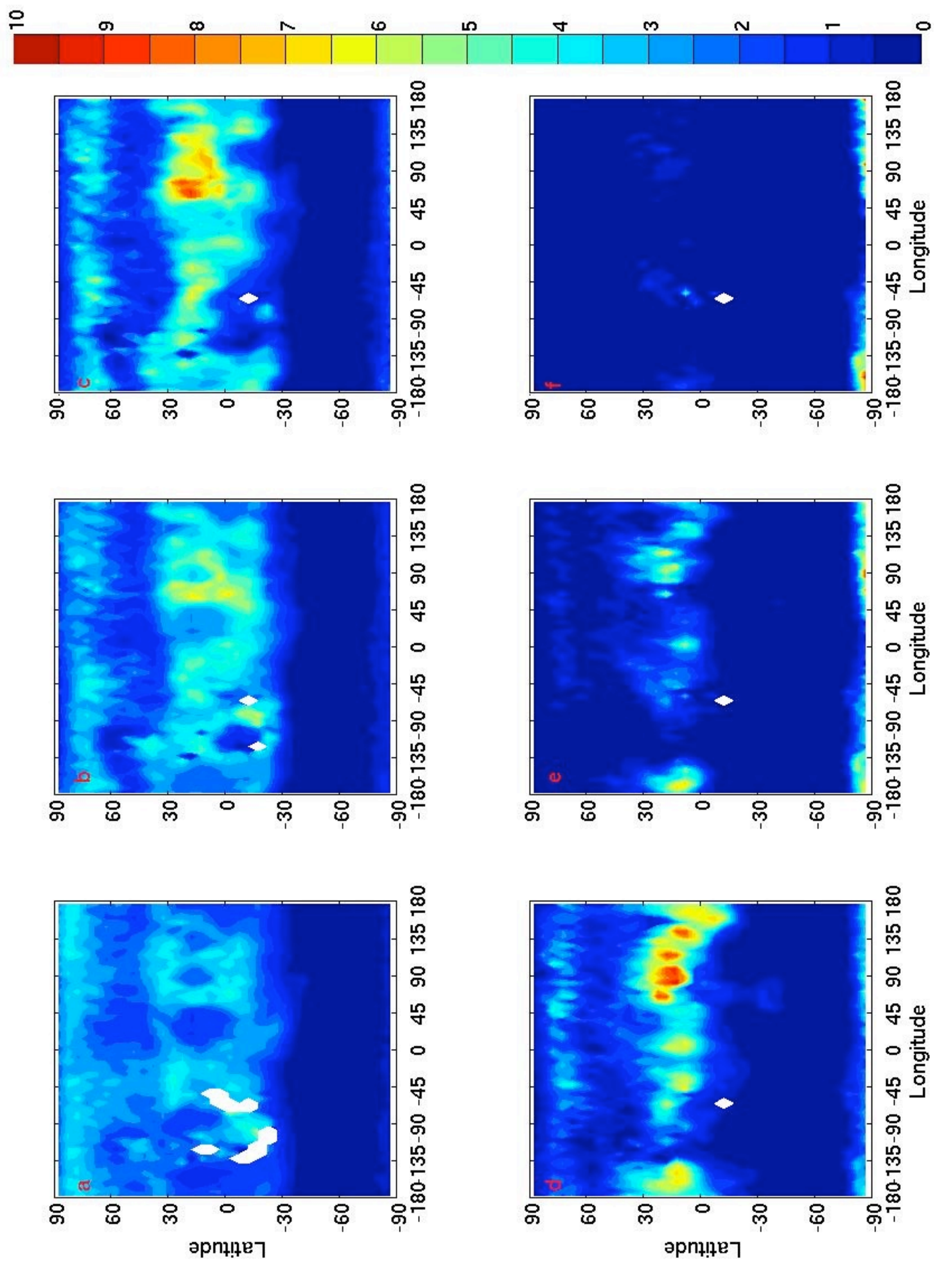

Figure 5.2. Average nightside dust density scaled opacity (L_s=75°-105°) on σ levels equivalent to: (a) 1; (b) 1.5; (c) 2; (d) 2.5; (e) 3; (f) 3.5 “scale heights” above the surface.

near the south pole (CO_2 ice) and over Hellas (40° S, 45°—90° E) in Figure 5.2d. Dust density scaled opacity in the tropics generally increases with altitude above the surface in Figures 5.2b-c, except near Arsia Mons and Syria Planum (0°—15° S, 135°—45° W), where the atmosphere grows clearer. The tropics clear with higher altitude above the surface (Figures 5.2d-f). The highest average dust density scaled opacities are found at 2.5—3 scale heights above the surface in the northern tropics near 60°—135° E, a broad region that spans Syrtis Major, Isidis Planitia, and western Elysium Planitia.

5.3.3 Temporal Variability in the Dust Distribution near the Northern Tropic

The pattern of longitudinal variability derived from the relatively long-term average in Figure 5.2 also can be extracted from averaging over shorter periods. Retrieval coverage is sufficiently good that longitudinal cross-sections can be constructed from interpolation of all retrievals in a narrow latitudinal and L_s range (2º in both cases) with a resolution of ~10º of longitude. Figures 5.3—5.6 show such cross-sections for a narrow latitudinal band around the northern tropic, which intersects the Elysium Montes at ~150° E; comes close to the sites of the Mars Pathfinder and Viking Lander 1 sites at ~45° W; intersects Lycus Sulci at ~135° W; and roughly corresponds to the dustiest part of the HATDM. In some cases, two nearly simultaneous retrievals are spaced by less than the thickness of the latitudinal band and so appear close together. The dust distributions in these closely spaced retrievals are generally similar.

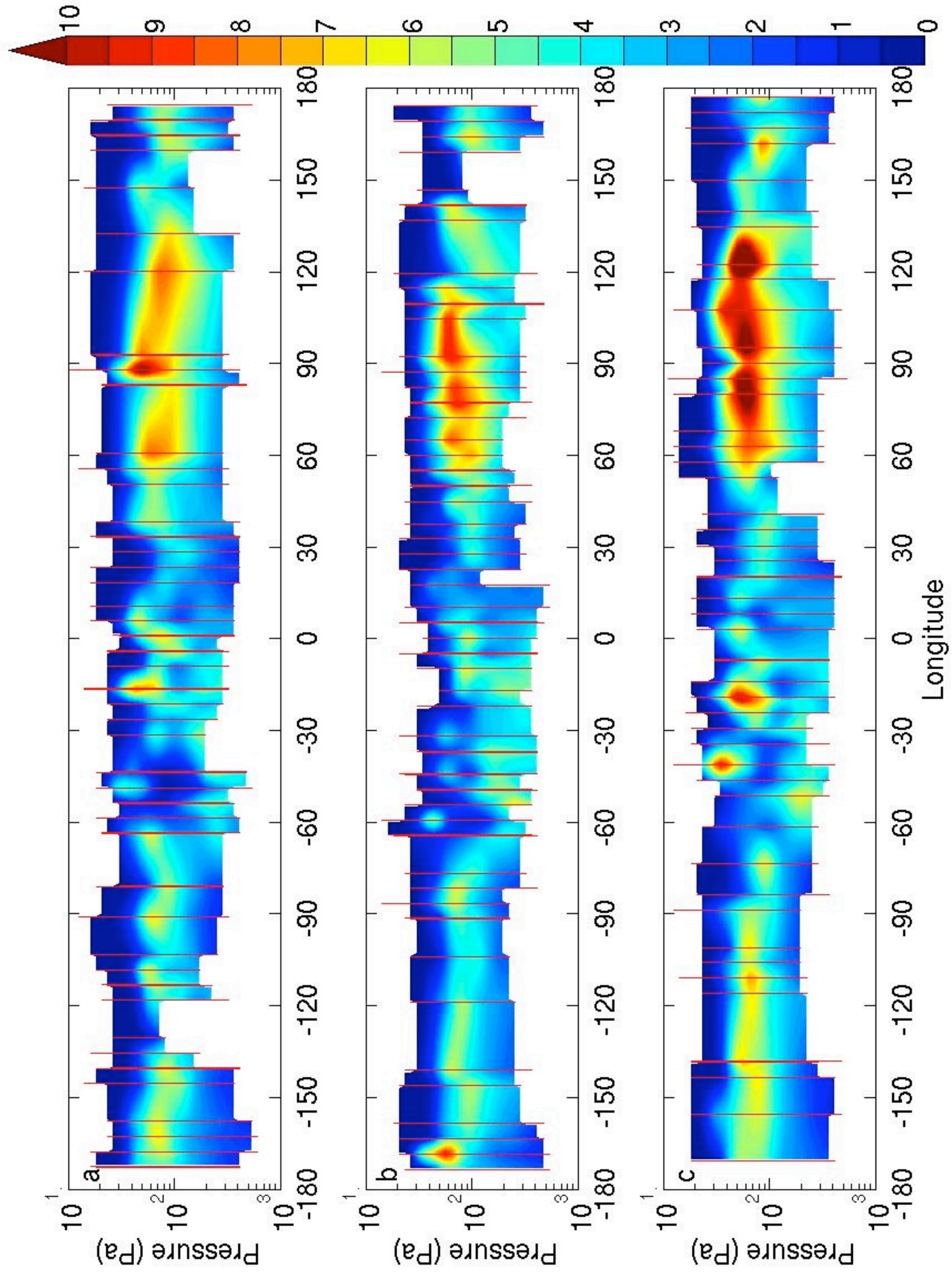

Figure 5.3. Interpolated cross-section of dust density scaled opacity*10^4 m^2 kg^{-1} for all nightside retrievals between 24.3°and 26.3° N over : (a) L_s=88°—90°, MY 29; (b) 78°—80°, MY 29; (c) 98°—100°. The mean longitude of each retrieval and the vertical range on which dust was retrieved is marked with a red line.

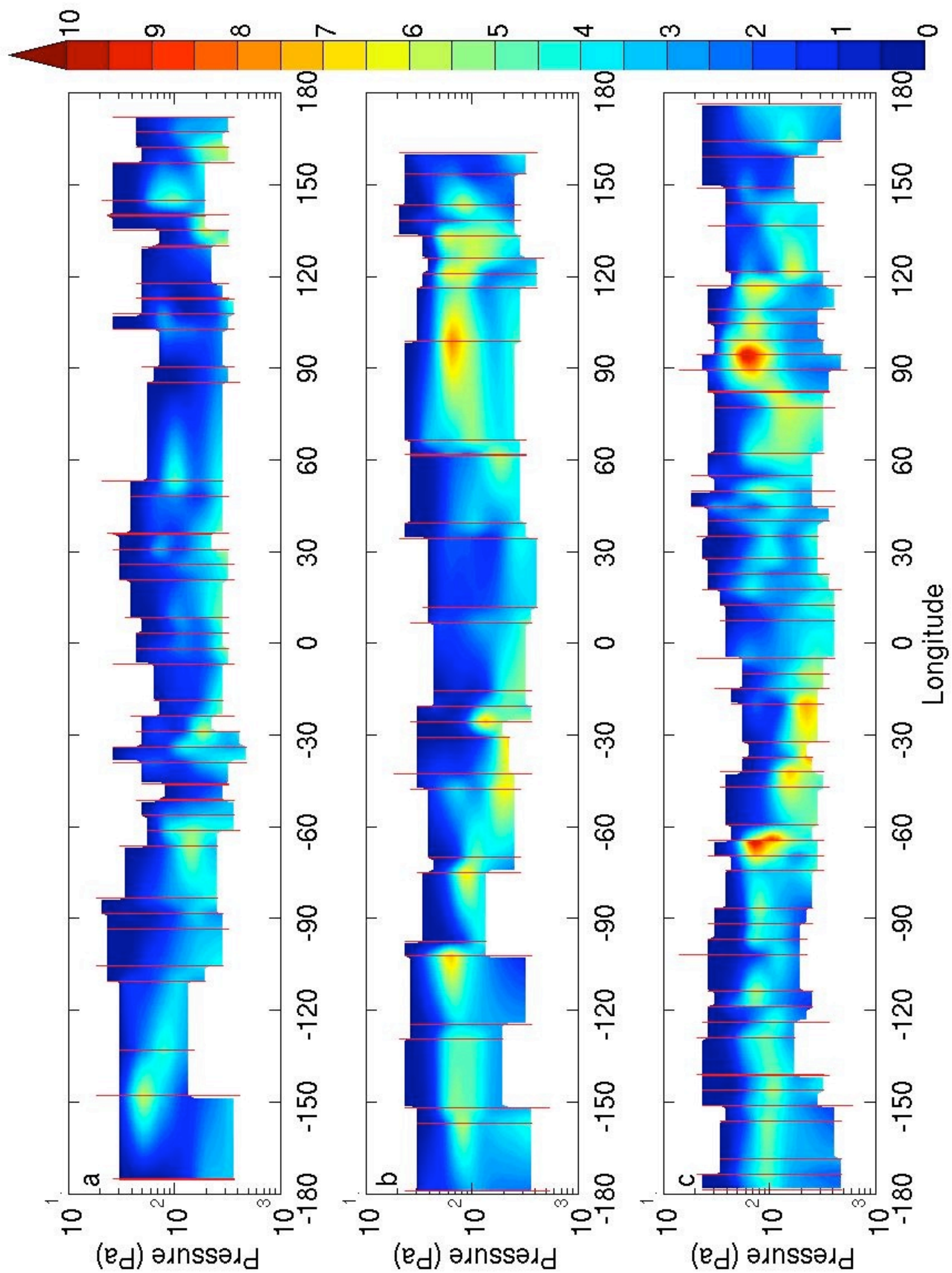

Figure 5.4. Interpolated cross-section of dust density scaled opacity*10^4 m^2 kg^{-1} for all nightside retrievals between 24.3°and 26.3° N over: (a) L_s=36°—38°, MY 29; (b) 44°—46°, MY 29; (c) 50°—52°, MY 29. The mean longitude of each retrieval and the vertical range on which dust was retrieved is marked with a red line.

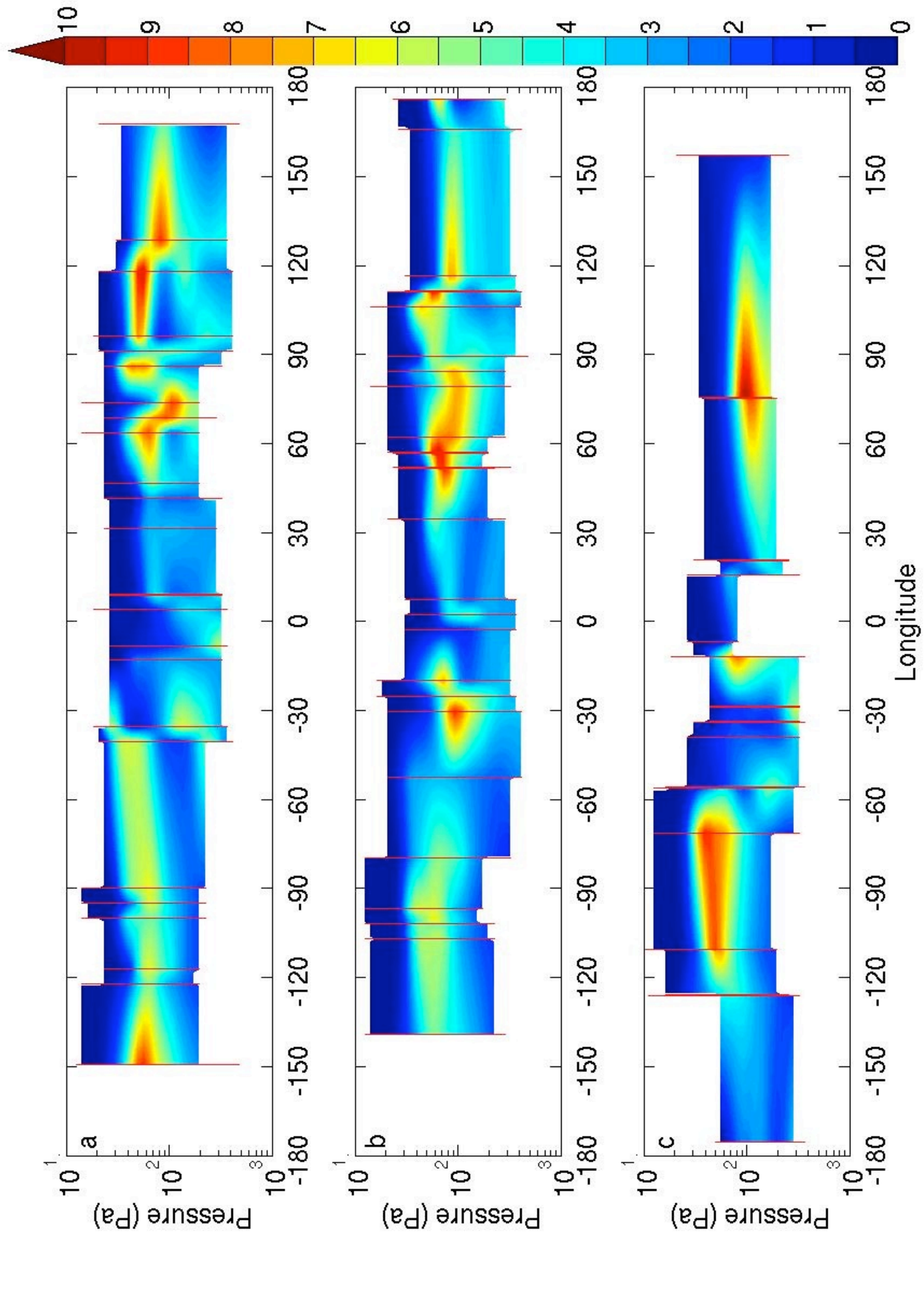

Figure 5.5. Interpolated cross-section of dust density scaled opacity*10^4 m^2 kg^{-1} for all nightside retrievals between 24.3° and 26.3° N over : (a) L_s=132°-—134°, MY 29; (b) 134°—136°, MY 29; (c) 138°—140°. The mean longitude of each retrieval and the vertical range on which dust was retrieved is marked with a red line.

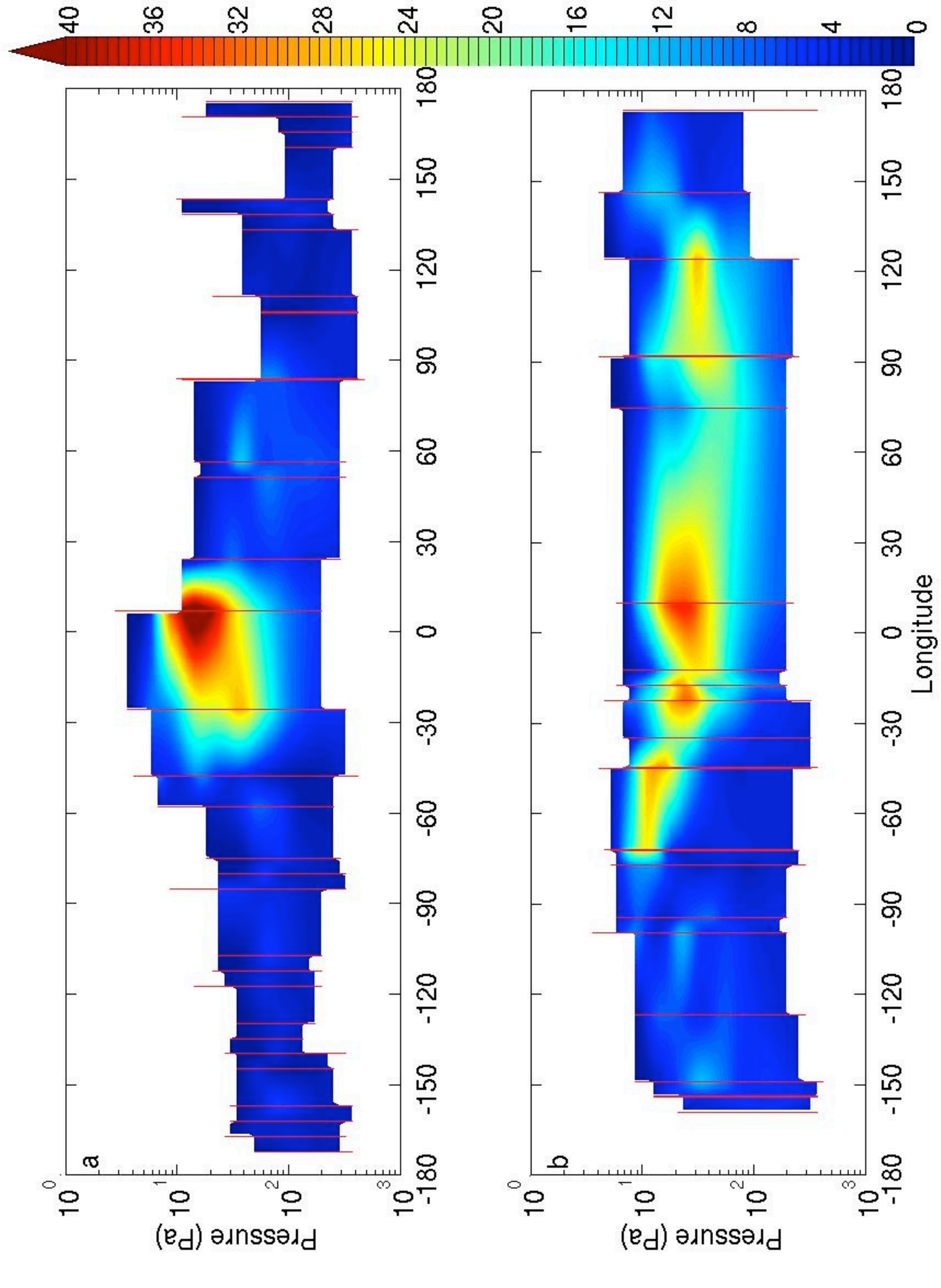

Figure 5.6. Interpolated cross-section of dust density scaled opacity (10^{-4} m^2 kg^{-1}) for all nightside retrievals between 24.3° and 26.3° N over : (a) L_s=142°—144°, MY 29; (b) 146°—148°, MY 29. The mean longitude of each retrieval and the vertical range on which dust was retrieved is marked with a red line.

Figures 5.3a-c show the longitudinal dust distribution at northern summer solstice and 10° of L_s before and after. The striking feature is how similar the distributions over this period. There is an enriched layer of dust that spans 30° E to 50° W at ~80 Pa. This layer has especially high dust density scaled opacity between 60° and 135° E. The area without the enriched layer generally has more dust at higher pressure levels than the rest of the longitudinal band but can have enriched layers of dust discontinuous with the broader enriched layer.

Figures 5.4a-c shows that a qualitatively similar longitudinal dust distribution first emerges around L_s=40° during MY 29. The distribution may be losing this character at around L_s=135° (Figures 5.5a-c). A longitudinally broad enriched layer emerges at this latitudinal band again at around L_s=140°, but this layer is much higher in dust density scaled opacity and reaches lower pressure levels (as low as 10 Pa). Thus, the characteristic longitudinal pattern of dust at northern summer solstice persists during the exact same period during which the HATDM persists (see Chapter 4). Note that the change between Figures 5.5c, 5.6a, and 5.6b occur over the course of 6° of L_s, a much briefer period than that which separates Figures 5.3b and 5.3c. Therefore, the dust distribution around northern summer solstice is remarkably static in comparison with the distribution later in the summer.

5.3.4 Discussion

Not only is the longitudinal dust distribution within the HATDM relatively static, it is statically inhomogeneous, both longitudinally and as an enriched layer in the vertical. Presumably, on some characteristic timescale, the longitudinal distribution would be homogenized by advection, while the vertical distribution would be homogenized (made more uniform) by sedimentation and vertical eddy diffusion. Yet it is not.

In the case of zonal advection, horizontal inhomogeneities should be smoothed on a timescale equivalent to ratio of the circumference of the latitude circle (~2×10^7 m) to the characteristic zonal wind speed at the level of the enriched layer (10—20 ms^{-1} easterly [*Forget et al.*, 1999]). This is equivalent to 1—2×10^6 s. The sedimentation velocity under martian conditions is approximately:

$$v_s = \frac{kr}{\rho} \tag{5.1}$$

where k is a constant of proportionality (~15 kg s^{-1} m^{-3}), r is the particle radius, and ρ is the air density [*Murphy et al.*, 1990]. For 1 μm sized particles, Eq. 5.1 would predict sedimentation velocities of ~0.01 ms^{-1} at 20 km above the surface, which would decrease at lower altitudes. An enriched layer at 20 km would fall to 10 km and thereby become diluted within ~1—3×10^6 s. *Korablev et al.* [1993] estimate the vertical eddy diffusivity of the atmosphere in the tropics during early northern spring to be ~10^6 cm^2 s^{-1}, which corresponds to a vertical mixing time of ~4×10^6 s for the lower 20 km of the atmosphere. The timescale on which the dust distribution is static is at least ~3.9×10^6 s (the difference between the periods used for Figures 5.3b and 5.3c) and perhaps as great as 1.6×10^7 s (the difference between the periods used for Figures 5.4c and 5.5a). This timescale is thus either similar or greater than the timescales of advection, sedimentation, and vertical eddy diffusion, implying that this dust distribution is sustained by dust lifting, transport, and removal processes that effectively oppose advection, sedimentation, and eddy diffusion throughout late northern spring and early northern summer.

As noted in Chapter 4, the transition in the dust distribution at around L_s=140° is contemporaneous with a regional dust storm in the tropics observed by the Thermal Emission Imaging System (THEMIS) on Mars Odyssey and the Mars Color Imager (MARCI) on MRO. Longitudinal sampling is much poorer after this period, so cross-sections of similar quality to those in Figures 5.3—5.6 cannot be constructed in this latitudinal band until at least L_s=160°. I shall discuss in the next Section whether the enriched layer in Figures 5.6a-b is a signature of the dust storm activity observed by THEMIS and MARCI

5.4 Possible Causes of the HATDM

5.4.1 Approach

In this part of the Chapter, some processes that could produce the HATDM during northern spring and summer are discussed. In each case, the theoretical and observational basis for each process are reviewed and past work is supplemented with additional modeling where necessary. Where possible, I attempt to isolate the signature of the process within the MCS observations on the basis of previous or contemporaneous observational records. Finally, I evaluate whether the process is likely to be responsible the HATDM based on the available evidence. In most cases, the observational record and past modeling work are insufficient to determine if a process makes a significant contribution to the HATDM. In those cases, I identify what further modeling experiments or observations are needed.

5.4.2 Dust Storms

The potential for regional to planetary-scale dust activity to produce equatorial maxima in dust mass mixing ratio by entraining dust into a vigorous cross-equatorial Hadley cell is a well-known phenomenon in GCM and simpler three-dimensional simulations [e.g., *Haberle et al.*, 1982; *Newman et al.*, 2002b; *Kahre et al.*, 2008]. *Newman et al.* [2002b] simulates the evolution of a dust storm in Hellas that produces a zonal average dust mass mixing ratio profile with a maximum stretching from ~60° N to 60° S at 25—35 km of 10—15 ppm. The simulated maximum appears somewhat bifurcated, possibly due to the influence of a weak meridional cell in the southern high latitudes. But the high optical depth region of lifting is mainly restricted to Hellas and is extremely shallow, leaving a gap in mass mixing ratio between the lifting area at the surface and the maximum at 25—35 km.

Dust storms also could enhance the appearance of a maximum in dust mass mixing ratio above the surface in an average such as a zonal average. The retrieval algorithm does not attempt retrieve dust at altitudes at which the line-of-sight opacity is above 2.5 (equivalent to ~0.05 km^{-1} in the retrieved profile) [*Kleinböhl et al.*, 2009]. Assuming the air density at the surface is ~1.5×10^{-2} m^2 kg^{-1}, the limit on dust density scaled opacity near the surface is relatively high (~3.3×10^{-3} m^2 kg^{-1}), but scattering and potentially higher dust grain size near the surface may limit retrieval success or retrieval vertical range in the vicinity of dust storms. Retrievals of outflow from dust storms, which might contain enriched layers of dust at altitude (lower limb opacity), thus may be more successfully retrieved. The preferential inclusion of the retrievals of outflow in an average could create a local maximum in dust mass mixing ratio above the surface. Such

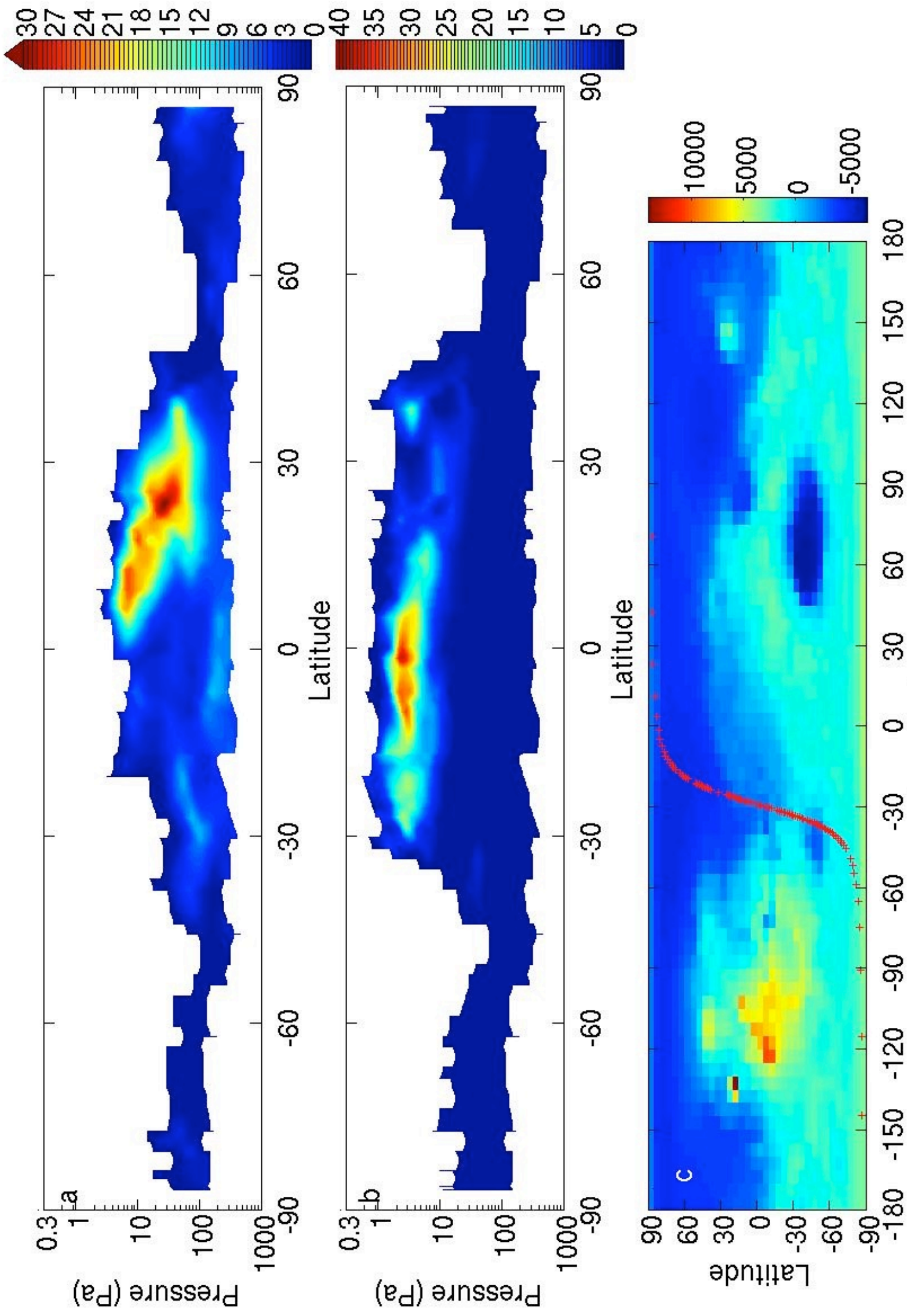

Figure 5.7. (a) and (b) Cross-sections of dust density scaled opacity (10^{-4} m^2 kg^{-1}) and water ice density scaled opacity (10^{-3} m^2 kg^{-1} from all available retrievals in a single nightside MRO pass on 16—17 October 2008 from 23:50 to 00:47 UTC (L_s=142.9412°—142.9612°, MY 29). (c) Mean latitude and longitude of each retrieval used in (a) and (b) (red crosses) on a topography (m) map (colors) based on MOLA data.

a maximum would be enhanced relative to a local maximum arising only from the averaging of retrievals of uniformly mixed dust profiles over regions of active lifting with retrievals of detached dust hazes in the outflow of the dust storm.

Enriched layers of dust attributable to dust storm outflow can be observed in MCS retrievals. Figures 5.7a-b show latitudinal cross-sections of dust and water ice density scaled opacity constructed from all nightside retrievals in a single orbit. This particular cross-section contains one of the retrievals used in Figure 5.6a and so effectively intersects it. The mean latitudes and longitudes of these retrievals are marked on a topography map in Figure 5.7c. In Figure 5.7a, there appears to be a haze of dust with density scaled opacity of up to 3×10^{-3} m^2 kg^{-1} over the northern tropics. Water ice clouds with density scaled opacity of up to 4×10^{-2} m^2 kg^{-1} are present south of this haze at pressure level similar to the lowest pressure level (~5 Pa) the dust haze penetrates. Based on the methods described in Chapters 4 and 6, the estimated dust mass mixing ratio is ~40 ppm, while the estimated water ice mass mixing ratio is up to 85 ppm, which is approximately a factor of 5 greater than the estimated zonal average water ice mass mixing ratio at this time of year (Chapter 6). The water ice mass mixing ratio of the cloud also is equivalent to a column-uniform water vapor mixing ratio of ~15 precipitable microns, the approximate zonal average column water vapor mixing ratio observed by the Compact Reconnaissance Imaging Spectrometer (CRISM) on MRO at this latitude and season [*Smith et al.*, 2009].

The observations in Figure 5.7 were made on 16—17 October 2008. *Malin et al.* [2008a] report that during the week of 13—19 October 2008 “water ice clouds and diffuse dust from last week’s regional dust storm lingered over the MER-B landing site” at Meridiani Planum. While the observations in Figure 5.7 were made significantly westward of Meridiani Planum, even higher dust concentrations were present along the northern tropic further east (Figure 5.6a). (The retrieval at ~10° E in Figure 5.6a does not have any successful retrievals near it in the same orbit that could confirm directly that this haze was present over Meridiani Planum.) *Malin et al.* [2008a] also report dust storm activity in Chryse Planitia during this week. Since dust concentrations are relatively low at the longitude of Chryse Planitia (~60° W) in Figure 5.6a, we propose that the dense dust hazes in Figures 5.6a and 5.7a are the result of advection of dust from "last week's regional dust storm" reported by *Malin et al.* [2008a], which moved from Solis Planum to Noachis Terra during the previous week [*Malin et al.*, 2008b].

The high density scaled opacities of the water ice clouds that trail the haze are consistent with this idea. The estimated water vapor equivalent of these clouds is close to the measured column mixing ratio of water vapor, suggesting that water vapor was very deeply mixed in the atmosphere, which is a potential result of water vapor being transported to high altitudes within the advected dust plume.

If the dust haze was advected across the equator, the direction of transport was opposite to the sense of the modeled mean meridional circulation in northern summer [e.g., *Richardson and Wilson*, 2002], in which meridional transport above the surface is north to south. Therefore, it is possible that the dust was advected in a longitudinally restricted circulation with flow opposite to the mean meridional circulation. Such a circulation could be explained by invoking a strong diabatic heat source in the southern tropics, such as the storm that was the source of the enriched dust layer. In summary,

Figure 5.7 seems to show a spectacular example of outflow from a dust storm producing an apparent maximum in dust mass mixing ratio at high altitude above the surface.

Dust storm outflow, however, is not a good explanation for the HATDM in late northern spring and early northern summer, because dust storm activity is relatively rare in the tropics during this period. *Cantor et al.* [2001] presents a detailed climatology of local dust storm activity in 1999. This study lacks coverage in northern spring and early northern summer, during which the tropical maximum in mass mixing ratio is most pronounced. But *Cantor et al.* [2001] does present results from earlier studies using Viking Orbiter data that are consistent with the presence of very few dust storms in or near the tropics around the summer solstice. Some local dust storm activity is observed at around L_s=110° just northwest of Elysium Mons, but activity at other longitudes on the edge of the northern tropics is relatively rare until northern fall. *Cantor et al.* [2006] presents a less detailed but interannual climatology of dust storm activity over most of the period of Mars Orbiter Camera (MOC) observations and shows that local dust storm activity around northern summer solstice is generally confined to the polar cap edges, especially in the northern hemisphere. Therefore, if local dust storms are responsible for the tropical maximum in mass mixing ratio, only a small number of dust storms could be involved.

The THEMIS optical depth measurements [*Smith*, 2009] provide further support for the absence of dust storms in the tropics. Cap edge dust storm activity in the northern hemisphere generally has zonal average 1065 cm^{-1} optical depths of 0.1—0.3. The tropical dust storm activity in mid to late northern summer of MY 29 is associated with zonal average optical depths of 0.3—0.5 or greater. Zonal average optical depth at 30°-40° N and throughout the tropics is generally 0.05—0.10 through northern spring and summer, which appears to be too low to indicate dust storm activity.

I also have considered the possibility that outflow from north cap edge dust storm activity might be advected into the tropics. Such a plume probably would have to cross the transport barrier due formed by the southerly flow and downwelling due to a secondary PMOC [*Richardson and Wilson*, 2002]. This barrier may be manifested by a region of lower dust density scaled opacity at ~45° N in Figure 5.1a and a mostly longitudinally uniform band of lower dust concentrations at a similar latitude in Figure 5.2. Moreover, the average dust density scaled opacities around the northern cap edge are somewhat lower than those observed in the tropics (Figure 5.2), so it seems unlikely that the northern cap edge activity could be a source of dust for the HATDM.

5.4.3 Orographic Circulations

There are many reasons why high altitude locations on Mars might or might not be unusually active sites for dust lifting. The main argument against dust lifting at high altitudes is that the threshold wind velocity for dust lifting is inversely proportional to the square root of density. This effect may be compensated in part by the higher winds that generally occur at higher altitudes. In addition, pressures at the high altitudes of Mars are on the rapidly increasing portion of the Päschen curve of CO_2, which may permit stronger electric fields than at lower altitudes and enhanced dust lifting by electrostatic effects [*Kok and Renno*, 2006]. Yet concerns about the difficulty of lifting dust from mountain tops may be irrelevant to the role of orography in the dust cycle, since mountains on Mars might act as a means for dust to be lifted at lower altitudes but injected into the atmosphere at higher altitudes.

The proposed dynamics of orographic injection of dust are fairly simple. During the daytime, the air on the top of the mountain heats more quickly than the air at the bottom of the mountain due to the lower density of the air at the top of the mountain. In addition, the air in contact with the surface of the mountain (either summit or slope) is warmed more quickly than the air at the same altitude away from the mountain. The heated mountain therefore becomes a local center of low pressure, producing a convergent anabatic wind that lifts dust from the slopes and makes the air at the top of the mountain very dusty and even hotter. Simulations by *Rafkin et al.* [2002] of a cloud and hypothetically connected orographic thermal circulation on Arsia Mons showed that the vertical velocities of the anabatic wind were up to 25 ms^{-1} and needed to be balanced by extremely strong (> 40 ms^{-1}) divergent winds at the top of the orographic circulation. The end result is advection of dust at levels on the order of a few ppm at ~20 km altitude at a distance up to 2000 km from the mountain. Such a process would be one plausible source for a HATDM.

The cloud type simulated by *Rafkin et al.* [2002] is called a "mesoscale spiral cloud." This type may be identical to or genetically related to the "aster clouds" observed by *Wang and Ingersoll* [2002]. Aster clouds form in late northern summer or early northern fall, are 200—500 km long, 20—50 km wide, and are found at altitudes of 15 km or more above the surface. Both types of clouds are thought to be generated by strong upslope winds. As of yet, there is no sufficiently detailed climatology of mesoscale spiral clouds or aster clouds to permit direct comparison with MCS retrievals.

Moreover, the present MCS retrieval dataset is not ideal for isolation of orographic cloud dynamics for three key reasons. First, the dearth of dayside equatorial profiles in the tropics throughout much of northern spring and summer limits information about the aerosol distribution over the volcanoes at the time of day and season when the upslope winds are thought to be most active. Second, both observations and modeling [*Benson et al.*, 2006; *Michaels et al.*, 2006] suggest that orographic water ice clouds are strongly entrained into the global wind field once they escape their local mesoscale circulations. Orographic dust clouds likely would be subject to the same effect and would tend to advect zonally. In that case, roughly synchronous (within a few minutes) observations over the volcano and at adjacent longitudes in the same latitudinal band could verify their orographic origins. Such observations would be one possible use of cross-track observations for an instrument on a polar-orbiting spacecraft. Third, if dust advected from the volcano is blown off at relatively shallow depths above the high elevation surface, the current retrievals do not reach close enough to the surface to "see" this dust.

As an example of what is currently possible, Figures 5.8a-e show the seasonal variability in the vertical dust distribution over Mars's five tallest volcanoes in order of increasing latitude (Arsia Mons, Pavonis Mons, Ascraeus Mons, Olympus Mons, and Elysium Mons) during MY 29. The extrapolated surface pressures of each retrieval are shown in order to indicate where retrievals are available and show that the profiles are over relatively high terrain (at least 9 km above the Mars Orbiter Laser Altimeter (MOLA) datum in all cases). An MCS retrieval, however, is an integration of information

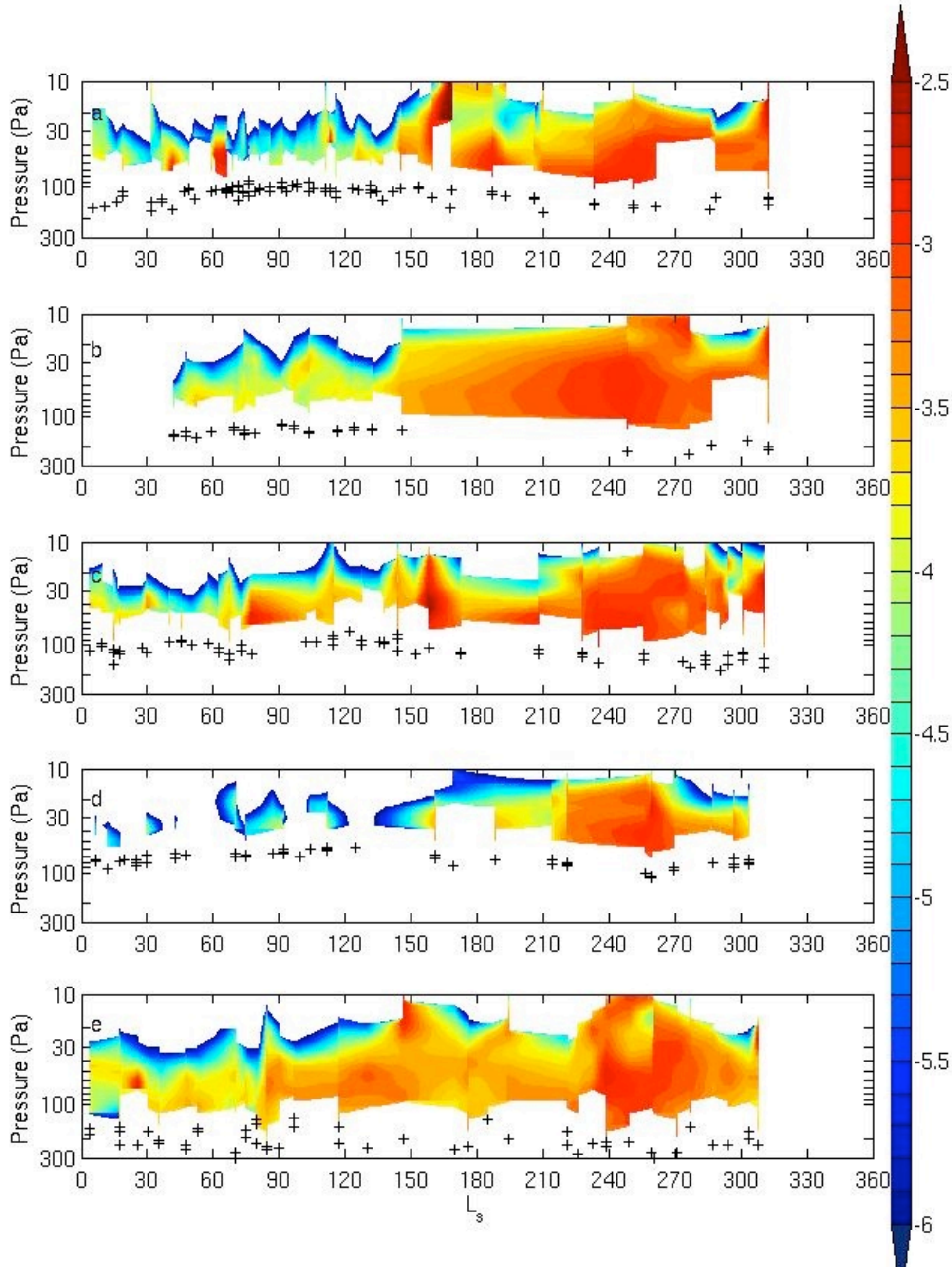

Figure 5.8. Log_{10} of dust density scaled opacity ($m^2\ kg^{-1}$) from both dayside and nightside retrievals. The black crosses indicate the L_s and extrapolated surface pressure for each retrieval: (a) near Arsia Mons (7.5°—11.5° S, 115.5°—125.5° W, estimated scene altitude of the profile > 15 km above the MOLA datum); (b) near Pavonis Mons (1.2° S—2.8° N, 108.4°—118.4° W, estimated scene altitude of the profile > 13 km above the MOLA datum); (c) near Ascraeus Mons (9.8°—13.8° N, 99.5°—109.5° W, estimated scene altitude of the profile > 15 km above the MOLA datum); (d) near Olympus Mons (16.4°—20.4° N, 129°—139° W, estimated scene altitude of the profile > 20 km above the MOLA datum); (e) near Elysium Mons (22.8°—26.8° N, 141.9°—151.9° E, estimated scene altitude of the profile > 9 km above the MOLA datum).

over a relatively broad volume, so Figures 5.8a-e should not be interpreted as equivalent to a record of narrow soundings above the volcano's summit by a balloon or a lidar.

The atmosphere above the volcanoes is dustier in southern spring and summer than in northern spring and summer, just like elsewhere in the tropics (Figure 5.1). In northern spring and summer, the dust distribution over each volcano resembles the dust distribution at the latitude of the volcano if it were cut off at higher pressures, followingthe general pattern of the HATDM, which is dustier and present at lower pressures in the northern tropics than the northern tropics. This contrast can be seen at ~60 Pa during northern spring and much of northern summer. Elysium Mons is much dustier than Pavonis Mons (Figures 5.8e and 5.8b). Olympus Mons (Figure 5.8d) has a very high surface, so retrievals do not reach pressures higher than ~40 Pa. In the zonal average (Figure 5.1), Mars is relatively free of dust at that pressure at this latitude and season, so Olympus Mons is relatively free of dust. In a few exceptional cases, high dust density scaled opacities are observed over the volcanoes at ~60 Pa, the approximate pressure of the HATDM.

Based on the available evidence, orographic injection is not a likely contributor to the HATDM. If aster clouds are the primary means of dust injection, their climatology (as presently known) differs from the HATDM. Like tropical dust storm activity, aster clouds occur too late in northern summer. Moreover, if orographic injection were primarily responsible for the HATDM, longitudinal inhomogeneities in the dust distribution likely should take the form of higher dust density scaled opacities downwind and nearer the volcano than upwind and further away. In Figure 5.3, the cross-sections may sample the modeled and observed path along which water ice clouds over Olympus Mons advect [*Benson et al.*, 2006; *Michaels et al.*, 2006], which is north and west of Olympus Mons (134° W). The cross-section likewise intersects Elysium Mons at ~147° E. Yet the enriched dust layer is of similar density scaled opacity on both sides of Olympus Mons and indeed density scaled opacity is usually at least half as high around Elysium Mons than at 60°—120° E. Orographic injection also does not explain the enriched layers of dust in individuals retrievals at 20°—40° W in Figure 5.2c, a location distant from significant topography.

Despite poor evidence for the mechanism causing the HATDM, the parsimony of orographic injection, however, remains attractive. The simplest way of explaining a layer of dust at 20 km above the mean altitude of the surface is that it comes from a surface 20 km above the mean. As long as the observational record of dust clouds over volcanoes is sparse and the daytime dust distribution over or near volcanoes remains poorly known, an orographic source for the HATDM cannot be fully disproven. Past modeling experiments have focused on the dust transport out of mesoscale circulations around volcanoes. Future experiments should simulate the contributions of these circulations to the global dust distribution in greater detail.

5.4.4 Dust Pseudo-Moist Convection

Dust devils are an attractive possible source for the HATDM, since they are thought to be the dominant mechanism for lifting dust under relatively clear conditions. *Fuerstenau* [2006] has proposed that solar heating of the dust load within a dust devil plume could result in a type of pseudo-moist convection, in which solar heating of the dust load exceeds adiabatic cooling of the parcel. Dust devil plumes therefore might be capable of breaking through the top of the boundary layer and detraining significant amounts of dust at altitude.

To supplement simple calculations of *Fuerstenau* [2006], which neglect the important process of entrainment of environmental air into dusty parcels, the single column cloud model of *Gregory* [2000] was modified to simulate the ascent of dust parcels. The model of *Gregory* [2000] has been successful in representing both shallow and deep cumulus convection on the Earth. In our model, a parcel with a given initial dust concentration, q_0, is in thermal equilibrium with the environment and has some initial vertical velocity, w_0 at the surface (z=0). Kinetic energy is defined as:

$$K = \frac{1}{2} w^2 \tag{5.2}$$

and the temperature of the parcel is allowed to evolve discretely in the height domain:

$$T(z + \Delta z) = T(z) - \left(\frac{\mathrm{g}}{\mathrm{c_p}} \Delta z \right) + \left[\frac{\Delta z}{w(z)} \varepsilon F_0 \cos\xi \exp(-\tau(z)/\cos\xi) \left(\frac{q(z)}{\mathrm{c_p}} \varsigma \right) \right] \tag{5.3}$$

where g is the acceleration due to gravity, c_p is the heat capacity, Δz is the resolution of the height grid, ξ is the solar zenith angle, is the efficiency of absorption of solar radiation by dust (including scattering), F_0 is the top of the atmosphere flux, τ is the environmental optical depth in the solar band, and ς is the conversion factor between mass mixing ratio and density scaled opacity in the solar band.

The buoyancy is then defined as:

$$B = g \frac{T_p - T_{env}}{T_{env}} \tag{5.4}$$

and the entrainment rate, E, is parameterized as:

$$E(z+\Delta z) = \frac{k_e}{w(z)^2} B(z+\Delta z)$$

(5.5)

where k_e is a constant. *Gregory* [2000] estimate the value of this constant to be ~0.045 for deep cumulus convection and ~0.09 for shallow cumulus convection.

The cooling of the temperature of the parcel and dilution of the dust mass mixing ratio by entrainment of environmental air is then represented as:

$$T_p^* = \frac{\left(E\Delta z T_{env} + T_p\right)}{1+E\Delta z}, \qquad q_p^* = \frac{\left(E\Delta z q_{env} + q_p\right)}{1+E\Delta z} \tag{5.6a-b}$$

if $E > 0$, where the starred quantities denote the transformed quantities after entrainment.

Finally, K is allowed to evolve:

$$K(z+\Delta z) = \left[K(z) + \mathrm{a}B(z+\Delta z) - (2\mathrm{b}DK(z)) - (2E(z)K(z))\right]\Delta z \tag{5.7}$$

where a and b are constants derived from large eddy simulations of terrestrial convection, and are estimated to be 1/6 and 0.5 respectively. D is the detrainment rate, which we assume to be zero when $E > 0$ and equal to $-E$ when $E < 0$. This may be an underestimate.

The total Convective Available Potential Energy (CAPE) is then estimated as:

$$CAPE = \int_0^{z_{LNB}} B dz \tag{5.8}$$

where z_{LNB} is the level of neutral buoyancy.

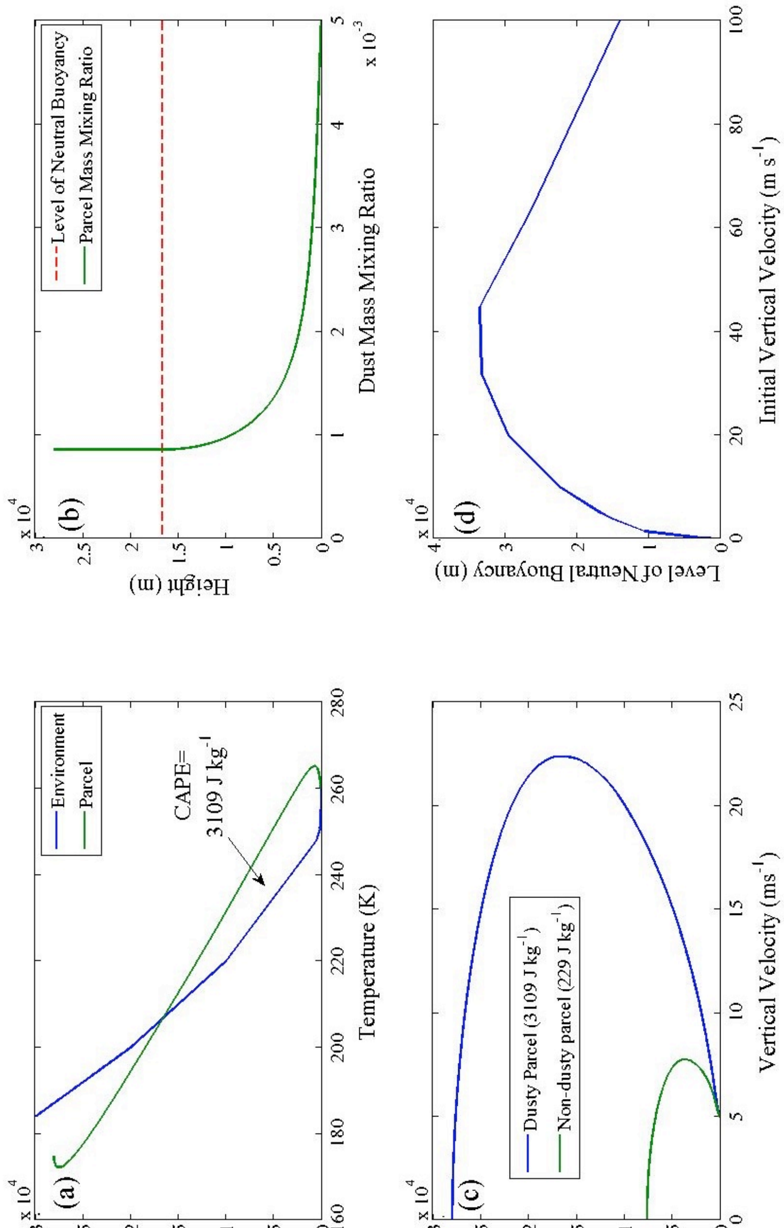

Figure 5.9. Results of simulations of dusty parcels at the Mars Pathfinder site: (a) parcel temperature profile vs. environmental temperature profile; (b) dust mass mixing ratio vs. height; (c) vertical velocity profile of a dusty parcel vs. a dustless parcel; (d) sensitivity of the level of neutral buoyancy to the assumed initial vertical velocity.

Table 5.1. Environmental temperature profile used for the single column model simulations of dust-heated convection

Height (m)	Temperature (K)
0	260
100	251
500	248
1,500	245
10,000	220
20,000	200
30,000	184
40,000	174
50,000	165

Table 5.2. Parameters for the single column model simulations of dust-heated convection

Parameter	Value	Citation (if any)
G	3.73 ms^{-2}	N/A
c_p	756 J kg^{-1}	N/A
ς	482 m^2 kg^{-1}	N/A
Δz	10 m	N/A
p_s	670 Pa	*Schofield et al.* [1997]
q_0	$5*10^{-3}$	*Metzger et al.* [1999]
w_0	5 ms^{-1}	N/A
τ_0	0.2	N/A
ν	0.1	N/A
k_e	0.09	*Gregory* [2000]
F_0	499 Wm^{-2}	N/A
ε	0.11	*Tomasko et al.* [1999]
ξ	11.8°	N/A

Figures 5.9a-d show the results of a single column simulation using Eqs. 5.2—5.8 of hypothetical dust parcels associated with dust devils observed near the Mars Pathfinder site ~12:40 LST (9:30 UTC) on 15 July 1997 (L_s=148.15°) [*Metzger et al.*, 1999; *Fuerstenau*, 2006]. The environmental temperature profile (Table 5.1) is based on Mars Pathfinder observations, temperature retrievals from the Miniature Thermal Emission Spectrometer, and L_s=145°—150° zonal average temperatures at the approximate latitude of Mars Pathfinder during MY 29 from MCS retrievals. The other parameters of the simulation are given in Table 5.2.

Figure 5.9a shows environmental and parcel temperature profiles of the simulation: a plot analogous to a SKEW—T diagram used in terrestrial weather forecasting. Note that the Convective Available Potential Energy (CAPE) of this parcel is comparable to strong terrestrial thunderstorm activity. The parcel is most strongly heated within the first couple of kilometers of ascent. Within the same height range, environmental temperatures decrease quickly in the superadiabatic layer near the strongly heated surface. At ~1,500 m, the approximate top of the boundary layer in this scenario, the dusty parcel is almost 20 K warmer than the external environment. The heating effect from the more dilute dust loading above ~2,500 m is not strong enough to keep the parcel from cooling more strongly than the environment. This strong gain in buoyancy near the surface relative to the rest of the path of ascent arises from the assumption that entrainment is inversely proportional to the square of velocity, so the parcel's dust concentration is strongly diluted by entrainment of environmental air when it is moving more slowly. On one hand, the low vertical velocity of the parcel enhances radiative heating relative to adiabatic cooling. On the other hand, it bleeds off dust through entrainment.

The effect of entrainment on the dust mass mixing ratio is significant. By ~5 km, the parcel has a mass mixing ratio of ~25% of its initial value (Figure 5.9b). Accounting for the fall off in density, the opacity of the parcel has fallen by a factor of six. By the level of neutral buoyancy, the mass mixing ratio has stabilized at ~20% of its initial value, but the relative opacity is ~5% of its initial value. One objection to the idea that dust devils are capable of dust injection at these heights is that dust devil heights from orbital surveys are no higher than ~8 km [*Fisher et al.*, 2005]. These height estimates, however, are based on the length of the dust devil shadow. To the best of my knowledge, the opacity limit for shadow detection is unknown, as is the effect of conservative mixing or entrainment with height on dust devil shadows.

In addition, any dust load of significant depth is subject to a self-shielding effect. The dust opacity near the surface in the simulated case is ~0.032 m^{-1}. So if the sun is at high elevation in the sky, only the top 30 m or so of the dust column are strongly heated and may detach somewhat from a primary plume of greater depth. If this detachment is primarily vertical, heating of the lower portion of the column will be limited, especially in the critical region of ascent through the superadiabatic layer. Comparison of the vertical velocity profile of a dusty parcel and a parcel without dust (equivalent to a fully shielded parcel) shows that such a shielded parcel would reach neutral buoyancy at ~3—4 km and cease ascent at ~7 km (Figure 5.9c), entirely consistent with observed dust devil heights. In the case of the shielded parcel, buoyancy is entirely derived from ascent through the superadiabatic layer, so weakening of this layer later in the day will limit the ascent of shielded parcels as well. These results suggest that the entire circulation of a dust devil probably does not penetrate the boundary layer. Instead, a number of small thermals detached by solar heating from the main dust devil plume ascend and then bring exceptionally dusty air (800—900 ppm in the simulated case) to 15—25 km altitude.

Figure 5.9d shows the sensitivity of the simulation results to the initial vertical velocity used and suggests that initial vertical velocities as low as ~2 ms^{-1} allow parcels to rise ~10 km. However, if the parcel rises too quickly, solar heating will not be able to compensate for adiabatic cooling, explaining the decay of the level of neutral buoyancy at high (and highly unrealistic) initial vertical velocity. In Figure 5.10, the conditions of the simulation were changed to consider the sensitivity of the results to initial dust mass mixing ratio of the parcel and initial vertical velocity. The colored contours conservatively plot the level of neutral buoyancy for each set of assumed conditions. The white contour marks 4 km, a typical tropical boundary layer height [*Hinson et al.*, 2008], and envelops a v-shaped phase space, in which the range of initial vertical velocities that can support boundary-layer breaking convection broadens with increasing initial mass mixing ratio. At the initial dust mass mixing ratio assumed in the simulation (~5,000 ppm), boundary-layer breaking convection can occur for initial vertical velocities less than 1 ms^{-1}. Thus, even dust plumes with relatively weak vertical velocities, which might arise from processes other than dust devils such as local circulations in craters etc., could be highly unstable with respect to pseudo-moist dust convection.

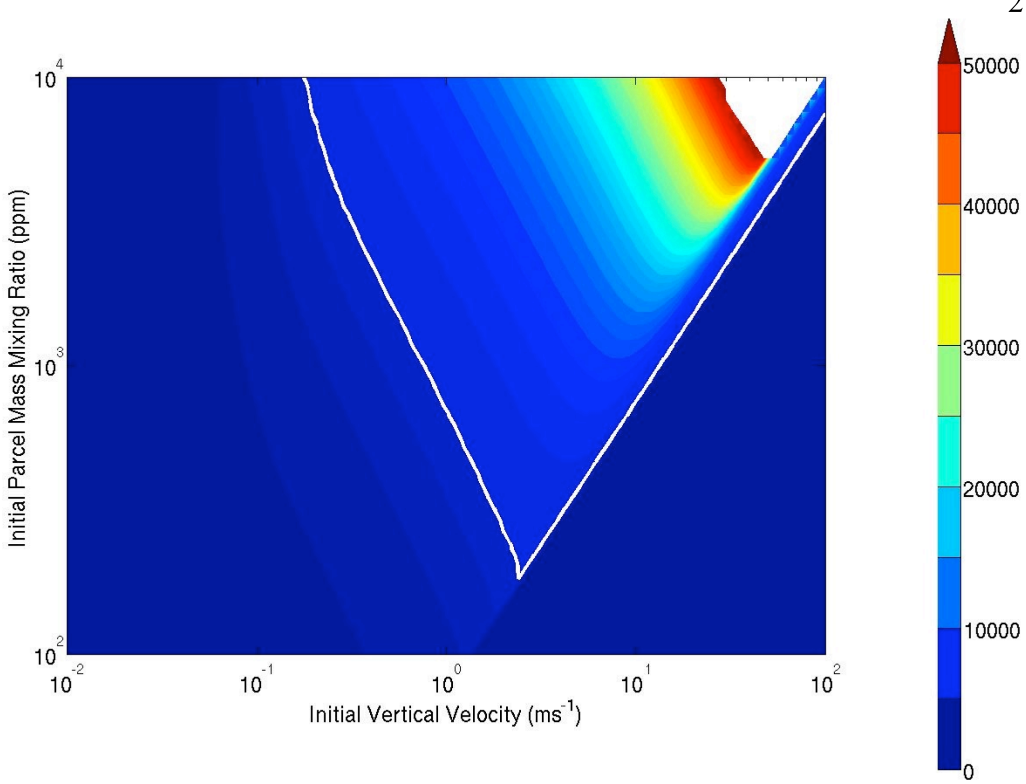

Figure 5.10. Sensitivity of level of neutral buoyancy (m) to initial parcel dust concentration (ppm) and initial parcel vertical velocity (ms^{-1}) The white line indicates the 4,000 m contour, the approximate boundary layer height of the simulation. The white area is indicative of simulations in which the parcel leaves the simulation domain.

Using the results from the simulation, the necessary vertical dust mass flux ($\hat{M}_{dust}$) to produce the HATDM can be estimated as:

$$\hat{M}_{dust} = \frac{\Delta p}{g}\frac{q_{excess}}{t_{sed}} \tag{5.9}$$

where Δp is the pressure thickness of the enriched layer, q_{excess} is the excess dust mass mixing ratio of the layer, and t_{sed} is the characteristic time of sedimentation/advection from the enrichment layer. Assuming Δp=85 Pa, g=3.73 ms^{-2}, q_{excess}=5×10^{-6}, and t_{sed} of ~10^{6} s, the necessary dust mass flux is: 1.1×10^{-10} kg m^{-2} s^{-1}. From this result and the results of the simulation, the fractional area occupied by these thermals ($f_{thermals}$) can be estimated to be:

$$f_{thermals} = \frac{\hat{M}_{dust}}{\frac{t_{thermals}}{t_{sol}}\rho w q_{thermal}} \tag{5.10}$$

Assuming that the thermals occur only ~10% of the day and w, $q_{thermal}$, and ρ correspond to their values at the level of neutral buoyancy of the simulated parcel (20 ms^{1}, 9×10^{-4}, and 4×10^{-3} kg m^{-3} respectively), the fractional area occupied by thermals needs only be 1.6×10^{-5}. Estimates of the fractional area occupied by dust devils range from 2×10^{-4}-6×10^{-4} [*Ferri et al.*, 2003; *Fisher et al.,* 2005], so the areal footprint of the thermals can be around an order of magnitude smaller than the areal footprint of dust devils.

This idea, however, is not observationally falsifiable with the MCS retrieval dataset. The purported boundary layer breaking dust plumes occur at scales much finer than the resolution of the observations. Moreover, comparison of dust devil climatologies with retrieved profiles of dust will not be a sufficiently unambiguous test for two reasons.

First, the two most complete surveys of dust devil activity on Mars disagree about fundamental aspects of the climatology. *Cantor et al.* [2006] analyze orbital imagery of dust devils and find that dust devils are far more common in the north than in the south. *Whelley and Greeley* [2008] analyzes orbital imagery of dust devil tracks and makes the opposite conclusion. Second, the sensitivity of pseudo-moist dust convection to parameters intrinsic to individual plumes such as initial vertical velocity and dust concentration (Figure 5.10) both raises the possibility that dust sources other than dust devils may drive pseudo-moist convection and also may introduce difficult to control intensity related biases in any correlation of dust devil climatologies and the vertical structure of dust.

Instead, the ease at which this effect can be demonstrated by our model and in the analysis of *Fuerstenau* [2006] suggests that this mechanism will become apparent in a mesoscale or large eddy simulation with rapidly updating radiative transfer. If this hypothesis is verified, parameterization within a GCM should be possible by upscaling from the smaller scale simulations. Observational validation likely will require lidar observations in the tropics in tandem with barometry, thermometry, and anemometry from a surface weather station.

5.5.5 Scavenging by Water Ice

Following Eq. 5.1, particles settle at a velocity in proportion to their radius. Eq. 5.1 is a simplification of an approximation of the Cunningham-corrected Stokes velocity at high Knudsen number ($Kn \approx 60$ for a 1 μm particle at the surface of Mars). The full approximation is:

$$v_s \approx \frac{4}{9}\frac{\rho_p r g \delta}{\rho v_t} \quad (5.11)$$

where δ is a slip-flow correction parameter and v_t is the thermal velocity of the gas [*Murphy et al.*, 1990]. Condensation of water ice on a dust particle will enhance its sedimentation velocity by increasing its radius. The new particle, however, will have a lower density. So if a 1 μm radius dust particle (ρ_p=3000 kg m^{-3}) grows into a 4 μm radius ice particle (the approximate r_{eff} in the aphelion cloud belt [*Clancy et al.*, 2003]), ρ_p of the new particle will be effectively the density of ice (~900 kg m^{-3}). Thus, the sedimentation velocity will increase by ~20%. If the ice particle is 2 μm in radius with a 1 μm radius core of dust, the sedimentation velocity is reduced by ~5%. Thus, if the ice particle sizes are close to the average water ice particle size observed from orbit, condensation of ice on dust does not significantly enhance sedimentation.

Using the Phoenix lidar, *Whiteway et al.* [2009] observed precipitating ice particles at ~ 4 km above the surface at night. Based on their sedimentation velocity, *Whiteway et al.* [2009] calculates that they could be ellipsoidal particles with a volume equivalent to a 35 μm radius sphere (or larger if columnar). Ice particles of this size may nucleate around multiple dust particles and will have sedimentation velocities about an order of magnitude greater than the sedimentation velocities of 1μm dust particles. If water ice clouds with particles of similar size to those observed by *Whiteway et al.* occur in the tropical atmosphere of Mars below the level of the HATDM, the scavenging of water ice by dust could create the appearance of a HATDM, subject to the condition that the vertical dust distribution before interaction with clouds is uniformly mixed to the altitude of the HATDM and the mass mixing ratio of this distribution is at least as great as the mass mixing ratio of the HATDM. In other words, dust is mixed to the height of the HATDM during the day and quickly scavenged during the night. In an isothermal atmosphere, the column opacity (τ) due to such a profile will be:

$$\tau = \int_0^{z_{HATDM}} DSO_{HATDM}\,\rho_s \exp(-z/H)\,dz \tag{5.12}$$

where z_{HATDM} is the characteristic altitude of the HATDM, DSO_{HATDM} is the characteristic dust density scaled opacity of the HATDM, and ρ_s is the air density at the surface. Eq. 5.12 integrates to:

$$\tau = DSO_{HATDM}\,\rho_s H\left(1-\exp\left[\frac{-z_{HATDM}}{H}\right]\right), \tag{5.13}$$

assuming $DSO_{HATDM}=5.5\times10^{-4}$ m^2 kg^{-1}, $H=10^4$ m, and $z_{HATDM}=2\times10^4$ m, τ=0.071. The visible column opacity corresponding to that column opacity in the A5 channel would be 0.52. Assuming the ratio between opacity in the 1075 cm^{-1} channel used for dust column opacity retrieval by THEMIS or TES and visible opacity is ~0.5, the implied column opacity of the pre-scavenged haze somewhat exceeds retrieved dayside column opacities at this latitude and season [*Smith*, 2004; *Smith*, 2009]. Yet without exact knowledge of the dust size distribution, converting an opacity in the MCS A5 channel to opacity in any other region of the spectrum is sufficiently uncertain that the observed dayside column opacities by TES and THEMIS could be consistent with a hypothetical pre-scavenged haze.

Another challenge to the possibility of scavenging is that the height of the HATDM exceeds the observed height of the convective boundary layer [*Hinson et al.,* 2008] by at least a factor of two. Thus, either the convective boundary layer is deeper than observed, the deep uniform mixing of the pre-scavenged profile is due to some process other than convective boundary layer overturning, or the pre-scavenged profile is not uniformly mixed. The first explanation is possible. *Hinson et al.* [2008] observes the boundary layer height in the northern tropics before the high altitude tropical maximum has reached its greatest altitude. *Hinson et al.* [2008] also observes in late afternoon, possibly after the boundary layer has reached its greatest depth. The second explanation is more unlikely. Some alternate form of mixing such as the solar heating of dust would need to be invoked. Yet such a process likely deepens the planetary boundary layer. The third explanation would either require a pre-existing vertical dust distribution with a local maximum in mass mixing ratio high above the surface or result in an unrealistically high column opacity.

Thus, within the present observational constraints, exceptionally deep dry boundary layer convection that entrains dust from systems such as dust devils and uniformly mixes this dust to high altitudes could generate the necessary pre-scavenged profile. The rarity of high quality dayside MCS retrievals in the tropics during northern spring and summer does not allow a systematic search for such uniformly mixed profiles. Yet this idea soon may be testable using column opacity retrievals from nadir and off-nadir views by MCS. The dayside dust column opacity could be used to simulate (based on considerations of uniform mixing) a pre-scavenged density scaled opacity limb profile. If scavenging is a significant process, nightside limb profiles in the vicinity of dayside dust column opacity measurements will be depleted in dust with respect to the simulated daytime limb profiles below the altitude of the HATDM.

5.5 Summary

The HATDM is a surprising feature of at least the nighttime vertical dust distribution of Mars for a quarter of its year. While enriched layers of dust at high altitudes above the surface during the rest of the year may be attributable to dust storms, the HATDM does not seem to be driven by dust storm activity. Instead, the existence of the HATDM may be evidence for the significant influence of processes related to topography, boundary layer circulations, and the water cycle on the global dust distribution during the "clear season." Since these processes are physically plausible at other seasons/latitudes, they may influence the dust distribution during the rest of the year.

Bibliography

Balme, M., and R. Greeley (2006), Dust devils on Earth and Mars, *Rev. Geophys.*, *44*, RG3003, doi:10.1029/2005RG000188.

Basu, S., M.I. Richardson, and R.J. Wilson (2004), Simulation of the Martian dust cycle with the GFDL Mars GCM, *J. Geophys. Res.*, *109*, E11006, doi:10.1029/2004JE002243.

Basu, S., J. Wilson, M. Richardson, and A. Ingersoll (2006), Simulation of spontaneous and variable global dust storms with the GFDL Mars GCM, *J. Geophys. Res.*, *111*, E09004, doi:10.1029/2005JE002660.

Benson, J. L., P.B. James, B.A. Cantor, and R. Remigo (2006), Interannual variability of water ice clouds over major Martian volcanoes observed by MOC, *Icarus*, *184*, 365–371, doi:10.1016/j.icarus.2006.03.014.

Cantor, B., M. Malin, and K. S. Edgett (2002), Multiyear Mars Orbiter Camera (MOC) observations of repeated Martian weather phenomena during the northern summer season, *J. Geophys. Res.*, *107*(E3), 5014, doi:10.1029/2001JE001588.

Cantor, B.A., P.B. James, M. Caplinger, and M.J. Wolff (2001), Martian dust storms: 1999 Mars Orbiter Camera observations, *J. Geophys. Res.*, *106*(E10), 23,653–23,687.

Cantor, B. A., K. M. Kanak, and K. S. Edgett (2006), Mars Orbiter Camera observations of Martian dust devils and their tracks (September 1997 to January 2006) and evaluation of theoretical vortex models, *J. Geophys. Res.*, *111*, E12002, doi:10.1029/2006JE002700.

Clancy, R. T., M. J. Wolff, and P. R. Christensen (2003), Mars aerosol studies with the MGS TES emission phase function observations: Optical depths, particle sizes, and ice cloud types versus latitude and solar longitude, *J. Geophys. Res.*, *108*(E9), 5098, doi:10.1029/2003JE002058.

Colaprete, A., J. R. Barnes, R. M. Haberle, and F. Montmessin (2008), CO2 clouds, CAPE and convection on Mars: Observations and general circulation modeling, *Planet. Space Sci., 56*(2), 150– 180.

Ferri, F., P. H. Smith, M. Lemmon, and N. O. Rennó (2003), Dust devils as observed by Mars Pathfinder, *J. Geophys. Res.*, *108*(E12), 5133, doi:10.1029/2000JE001421.

Fisher, J. A., M. I. Richardson, C. E. Newman, M. A. Szwast, C. Graf, S. Basu, S. P. Ewald, A. D. Toigo, and R. J. Wilson (2005), A survey of Martian dust devil activity using Mars Global Surveyor Mars Orbiter Camera images, *J. Geophys. Res.*, *110*, E03004, doi:10.1029/2003JE002165.

Forget, F., F. Hourdin, R. Fournier, C. Hourdin, O. Talagrand, M. Collins, S.R. Lewis, P.L. Read and J.-P. Huot (1999), Improved general circulation models of the Martian atmosphere from the surface to above 80 km, *J. Geophys. Res 104*, 24155–24175.

Fuerstenau, S. D. (2006), Solar heating of suspended particles and the dynamics of Martian dust devils, *Geophys. Res. Lett.*, *33*, L19S03, doi:10.1029/2006GL026798.

Gregory, D. (2000), Estimation of entrainment rate in simple models of convective clouds, *Q.J.R. Meteorol. Soc, 127*(571), 53-72.

Haberle, R.M., C.B. Leovy, and J.M. Pollack (1982), Some effects of global dust storms on the atmospheric circulation of Mars, *Icarus*, *50*, 322-367.

Haberle, R.M., J.B. Pollack, J.R. Barnes, R.W. Zurek, C.B. Leovy, J.R. Murphy, J. Schaeffer, and H. Lee (1993), Mars atmospheric dynamics as simulated by the NASA/Ames general circulation model I. The zonal mean circulation, *J. Geophys. Res., 98*, 3093-3124.

Hinson, D.P., M. Pätzold, S. Tellmann, B. Häusler, and G.L. Tyler (2008), Depth of the convective boundary layer on Mars, *198*(1), 57-66.

Kahn, R.A., T.Z. Martin, R.W. Zurek, and S.W. Lee (1992), The Martian Dust Cycle in H.H. Kieffer, B.M. Jakosky, C.W. Snyder, and M.S. Matthews, *Mars*, 1498 pp., University of Arizona Press, Tucson.

Kahre, M. A., J. R. Murphy, R. M. Haberle, F. Montmessin, and J. Schaeffer (2005), Simulating the Martian dust cycle with a finite surface dust reservoir, *Geophys. Res. Lett.*, *32*, L20204, doi:10.1029/2005GL023495.

Kahre, M. A., J. R. Murphy, and R. M. Haberle (2006), Modeling the Martian dust cycle and surface dust reservoirs with the NASA Ames general circulation model, *J. Geophys. Res.*, *111*, E06008, doi:10.1029/2005JE002588.

Kahre, M.A., J.L. Hollingsworth, R.M. Haberle, and J.R. Murphy (2008), Investigations of the variability of dust particle sizes in the martian atmosphere using the NASA Ames General Circulation Model, *Icarus*, *195*(2), 576-597.

Kleinböhl , A., J. T. Schofield, D. M. Kass, W. A. Abdou, C. R. Backus, B. Sen, J. H. Shirley, W. G. Lawson, M. I. Richardson, F. W. Taylor, N. A. Teanby, and D. J. McCleese (2009), Mars Climate Sounder limb profile retrieval of atmospheric temperature, pressure, dust, and water ice opacity, *J. Geophys. Res.*, *114*, E10006, doi: 10.1029/2009JE003358.

Kok, J. F., and N. O. Renno (2006), Enhancement of the emission of mineral dust aerosols by electric forces, *Geophys. Res. Lett.*, 33, L19S10.

Korablev, O. I., V. A. Krasopolsky, A. V. Rodin, and E. Chassefiere (1993), Vertical structure of the Martian dust measured by the solar infrared occultations from the Phobos spacecraft, *Icarus*, *102*, 76–87.

Malin, M. C., B. A. Cantor, T.N. Harrison, D.E. Shean and M.R. Kennedy (2008a), MRO MARCI Weather Report for the week of 13 October 2008 – 19 October 2008, Malin Space Science Systems Captioned Image Release, MSSS-55, http://www.msss.com/msss_images/2008/10/22/.

Malin, M. C., B. A. Cantor, T.N. Harrison, D.E. Shean and M.R. Kennedy (2008b), MRO MARCI Weather Report for the week of 6 October 2008 – 12 October 2008, Malin Space Science Systems Captioned Image Release, MSSS-54, http://www.msss.com/msss_images/2008/10/15/.

McCleese, D. J., J. T. Schofield, F. W. Taylor, S. B. Calcutt, M. C. Foote, D. M. Kass, C. B. Leovy, D. A. Paige, P. L. Read, and R. W. Zurek (2007), Mars Climate Sounder: An investigation of thermal and water vapor structure, dust and condensate distributions in the atmosphere, and energy balance of the polar regions, *J. Geophys. Res.*, *112*, E05S06, doi:10.1029/2006JE002790.

McCleese, D.J., J.T. Schofield, F.W. Taylor, W.A. Abdou, O. Aharonson, D. Banfield, S.B. Calcutt, N.G. Heavens, P.G.J. Irwin, D.M. Kass, A. Kleinböhl, W.G. Lawson, C.B. Leovy, S.R. Lewis, D.A. Paige, P.L. Read, M.I. Richardson, N. Teanby, and R.W. Zurek (2008), *Nature Geosci*., *1*, 745-749, doi:10.1038/ngeo332.

Metzger, S. M., J. R. Carr, J. R. Johnson, T. J. Parker, and M. T. Lemmon (1999), Dust devil vortices seen by the Mars Pathfinder Camera, *Geophys. Res. Lett.*, *26*(18), 2781–2784.

Michaels, T.I., A. Colaprete, and S. C. R. Rafkin (2006), Significant vertical water transport by mountain‐induced circulations on Mars, *Geophys. Res. Lett.*, *33*, L16201, doi:10.1029/2006GL026562.

Murphy, J. R., O. B. Toon, R. M. Haberle, and J. B. Pollack (1990), Numerical Simulations of the Decay of Martian Global Dust Storms, *J. Geophys. Res.*, *95*(B9), 14,629–14,648.

Newman, C. E., S. R. Lewis, P. L. Read, and F. Forget (2002a), Modeling the Martian dust cycle, 1. Representations of dust transport processes, *J. Geophys. Res.*, *107*(E12), 5123, doi:10.1029/2002JE001910.

Newman, C. E., S. R. Lewis, P. L. Read, and F. Forget (2002b), Modeling the Martian dust cycle 2. Multiannual radiatively active dust transport simulations, *J. Geophys. Res.*, *107*(E12), 5124, doi:10.1029/2002JE001920.

Putzig, N. E., M. T. Mellon, K. A. Kretke, and R. E. Arvidson (2005), Global thermal inertia and surface properties of Mars from the MGS mapping mission, *Icarus* 173, 325-341.

Rafkin, S. C. R., M. R. V. Sta. Maria, and T. I. Michaels (2002), Simulation of the atmospheric thermal circulation of a martian volcano using a mesoscale numerical model. *Nature*, *419*, 697-699.

Richardson, M.I. and R.J. Wilson (2002), A topographically forced asymmetry in the martian circulation and climate. Nature *416* (6878), 298-301.

Schneider, E.K. (1983), Martian Great Dust Storms: Interpretive Axially Symmetric Models, *Icarus*, *35*, 302-331.

Schofield, J. T., J. R. Barnes, D. Crisp, R. M. Haberle, S. Larsen, J. A. Magalhães, J. R. Murphy, A. Seiff, and G. Wilson (1997), The Mars Pathfinder Atmospheric Structure Investigation/Meteorology (ASI/MET) Experiment, *Science*, *278*, 1752–1758.

Smith, M. D. (2004), Interannual variability in TES atmospheric observations of Mars during 1999– 2003, *Icarus*, *108*, 148– 165.

Smith, M.D. (2009), THEMIS Observations of Mars aerosol optical depth from 2002—2008, *Icarus*, *202* (2), 444-452, doi:10.1016/j.icarus.2009.03.027.

Smith, M. D., M. J. Wolff, R. T. Clancy, and S. L. Murchie (2009), Compact Reconnaissance Imaging Spectrometer observations of water vapor and carbon monoxide, *J. Geophys. Res.*, *114*, E00D03, doi:10.1029/2008JE003288.

Strausberg, M. J., H. Wang, M. I. Richardson, S. P. Ewald, and A. D. Toigo (2005), Observations of the initiation and evolution of the 2001 Mars global dust storm, *J. Geophys. Res.*, *110*, E02006, doi:10.1029/2004JE002361.

Szwast, M. A., M. I. Richardson, and A. R. Vasavada (2006), Surface dust redistribution on Mars as observed by the Mars Global Surveyor and Viking orbiters, *J. Geophys. Res.*, *111*, E11008, doi:10.1029/2005JE002485.

Thomas, P. and P.J. Gierasch (1985), Dust Devils on Mars, *Science*, *230* (4722), 175-177.

Tomasko, M. G., L. R. Doose, M. Lemmon, P. H. Smith, and E. Wegryn (1999), Properties of dust in the Martian atmosphere from the Imager on Mars Pathfinder, *J. Geophys. Res.*, *104*(E4), 8987–9007.

Wang, H., and A. P. Ingersoll (2002), Martian clouds observed by Mars Global Surveyor Mars Orbiter Camera, *J. Geophys. Res.*, *107*(E10), 5078, doi:10.1029/2001JE001815.

Whelley, P. L., and R. Greeley (2008), The distribution of dust devil activity on Mars, *J. Geophys. Res.*, *113*, E07002, doi:10.1029/2007JE002966.

Whiteway, J. A., Komguem, L., Dickinson, C., Cook, C., Illnicki, M., Seabrook, J., Popovici, V., Duck, T. J., Davy, R., Taylor, P. A., Pathak, J., Fisher, D., Carswell, A. I., Daly, M., Hipkin, V., Zent, A. P., Hecht, M. H., Wood, S. E., Tamppari, L. K., Renno, N., Moores, J. E., Lemmon, M. T., Daerden, F., Smith, P. H. (2009) Mars Water-Ice Clouds and Precipitation, *Science*, *325* (5936), 68-70. doi: 10.1126/science.1172344.

Zurek, R.W., J.R. Barnes, R.M. Haberle, J.B. Pollack, J.E. Tillman, and C.B. Leovy (1992), Dynamics of the Atmosphere of Mars in H.H. Kieffer, B.M. Jakosky, C.W. Snyder, and M.S. Matthews, *Mars*, 1498 pp., University of Arizona Press, Tucson.